

# Evidence for cascaded third harmonic generation in non-centrosymmetric gold nanoantennas

*Michele Celebrano,<sup>1,‡,\*</sup> Andrea Locatelli,<sup>2,‡</sup> Lavinia Ghirardini,<sup>1</sup> Giovanni Pellegrini,<sup>1</sup> Paolo Biagioni,<sup>1</sup> Xiaofei Wu,<sup>3,4</sup> Swen Grossmann,<sup>3,4</sup> Luca Carletti,<sup>2</sup> Costantino De Angelis<sup>2</sup>, Lamberto Duò,<sup>1</sup> Bert Hecht,<sup>3,4</sup> Marco Finazzi<sup>1</sup>*

<sup>1</sup> Physics Department, Politecnico di Milano, Piazza Leonardo Da Vinci 32, 20133 Milano, Italy.

<sup>2</sup> Department of Information Engineering, University of Brescia, Via Branze 38, 25123 Brescia, Italy.

<sup>3</sup>Nano-Optics & Biophotonics Group - Department of Physics - Experimental Physics 5, University of Würzburg, Am Hubland, 97074 Würzburg, Germany.

<sup>4</sup>Röntgen Research Center for Complex Material Systems (RCCM), Am Hubland, 97074 Würzburg, Germany.

KEYWORDS Nonlinear optics, Plasmonics, Third Harmonic Generation, Second Harmonic Generation

## ABSTRACT

The optimization of nonlinear optical processes at the nanoscale is a crucial step for the development of nanoscale photon sources for quantum-optical networks. The development of innovative plasmonic nanoantenna designs and hybrid nanostructures to enhance optical nonlinearities in very small volumes represents one of the most promising routes. In such systems, the upconversion of photons can be achieved with high efficiencies via third-order processes, such as third harmonic generation (THG), thanks to the resonantly-enhanced volume currents. Conversely, second-order processes, such as second harmonic generation (SHG), are often inhibited by the symmetry of metal lattices and of common nanoantenna geometries. SHG and THG processes in plasmonic nanostructures are generally treated independently, since they both represent a small perturbation in the light-matter interaction mechanisms. In this work, we demonstrate that this paradigm does not hold in general, by providing evidence of a cascaded process in THG, which is fueled by SHG and sizably contributes to the overall yield. We address this mechanism by unveiling an anomalous fingerprint in the polarization state of the nonlinear emission from non-centrosymmetric gold nanoantennas and point out that such cascaded processes may also appear for structures that exhibit only moderate SHG yields – signifying its general relevance in plasmon-enhanced nonlinear optics. The presence of this peculiar mechanism in THG from plasmonic nanoantennas at telecommunication wavelengths allows gaining further insight on the physics of plasmon-enhanced nonlinear optical processes. This could be crucial in the realization of nanoscale elements for photon conversion and manipulation operating at room-temperature.

## INTRODUCTION

Since the first experimental evidences of enhanced nonlinear optical effects in nanostructured metals,<sup>1,2</sup> the field of nonlinear plasmonics has been experiencing a continuous growth<sup>3,4</sup> aimed at integrating multiple optical functionalities into ultra-compact all-optical devices.<sup>5</sup> Highly efficient nonlinear photon conversion in extremely confined volumes constitutes, indeed, a crucial step towards the realization of nanoscale photon conversion units<sup>6</sup> for quantum networks working at room temperature. In this frame, plasmonic nanoantennas can effectively compensate for the lack of phase-matching conditions<sup>7</sup> at the nanoscale by means of intense field enhancements and the steep field gradients generated by the antenna hotspots at the plasmon resonances.<sup>8,9</sup>

One of the most efficient upconversion mechanisms in plasmonics, Third Harmonic Generation (THG), consists in the absorption of three identical photons followed by the emission of a fourth photon at three times the energy of the impinging ones. For plasmonic nanoantennas working in the visible range, the emission yield of THG, stemming from the third-order nonlinear susceptibility,  $\chi^{(3)}$ ,<sup>10-14</sup> is commonly reported to be orders of magnitude higher than that of Second Harmonic Generation (SHG), which entails the emission of a photon at twice the energy of the two impinging ones and is mediated by the second-order nonlinear susceptibility,  $\chi^{(2)}$ . In fact, while  $\chi^{(3)}$  benefits from the resonantly-enhanced volume currents in plasmonic nanoantennas at visible wavelengths,  $\chi^{(2)}$  values are extremely small in the bulk of plasmonic materials due to the high degree of symmetry in their crystal structure. For this reason, SHG in plasmonics has been the subject of several studies over the last decades, which allowed determining the key role played by surface  $\chi^{(2)}$  processes stemming from the lack of inversion symmetry at the metal/environment interface<sup>15-22</sup>.

Despite its well-known bulk origin, the mechanisms at the basis of THG are still largely debated<sup>19-25</sup> and the experimental values of  $\chi^{(3)}$  in plasmonic materials are subject to extremely large uncertainties.<sup>25-28</sup> In particular, state-of-the-art modelling seems to fail in predicting the behavior of  $\chi^{(3)}$  in the near-infrared region,<sup>23-25</sup> where applications to sensing can profit from the low absorption of biological entities and nonlinear photon conversion would become compatible with optical fiber technology and silicon-based photonics. While according to the theoretical models a significant drop of  $\chi^{(3)}$  is expected in the near infrared, as also confirmed by recent experiments<sup>29</sup>, other experimental studies report extremely large THG conversion efficiencies in the same spectral range for both plasmonic<sup>10</sup> and hybrid nanoantennas<sup>30,31</sup>, indicating third-order nonlinear processes as the most promising route towards efficient photon conversion at the nanoscale. Further investigations are therefore essential to gain more insight into the processes promoting plasmon-enhanced THG in this wavelength range.

In this paper, we provide experimental evidence for the presence of a two-step cascaded process in the THG from non-centrosymmetric gold nanoantennas<sup>32</sup>, which adds to the THG originating from pure bulk currents. We ascribe this phenomenon to the Sum Frequency Generation (SFG) process occurring between a pump photon and a SHG photon, which is seeded by the surface  $\chi^{(2)}$  process. As predicted by full-wave simulations, the latter leaves a unique fingerprint in the THG polarization state, which deviates from that of a purely-bulk  $\chi^{(3)}$ -mediated effect. We unequivocally identify such behavior through the detection and analysis of the polarization states of both SHG and THG from the nanoantennas.

## MATERIALS AND METHODS

We focus onto two specific plasmonic nanostructures, realized following the same procedure as in Ref. 32 and depicted in the inset of Figure 1. The two antennas feature similar scattering cross-sections at the FW wavelength (1554 nm) and encompass a comparable volume, a choice that provides similar conditions for the bulk contribution to THG. Yet, while Antenna B is well-optimized to maximize SHG, the rod length of Antenna A is slightly detuned to provide less efficient SHG as can be inferred by their respective spectral response (see Figure 1). Based on these features and given the rather flat spectral response of both systems around the THG line of the pump laser, one would expect a marked change in the SHG and no significant variation of the THG from the two nanostructures.

We characterize and compare the nonlinear emission of the two nanostructures using the same microscopy setup employed in Ref. 32. The ultrafast pump pulses, emitted by an Er-doped fiber laser are linearly polarized (polarization ratio  $10^3:1$ ), to match the fundamental mode of the antenna (see Figure 1), and focused by a 0.85 numerical aperture (NA) air objective, resulting in a pump fluency ranging from 0.04 to 0.2 GW/cm<sup>2</sup> in the focal spot. The nonlinear emission is collected back by the same objective and, after a nonpolarizing beam-splitter and a filter cutting the residual pump radiation, is sent to either a visible/near infrared (Vis-NIR) spectrometer or a Single Photon Avalanche Detector (SPAD). The polarization state of the emitted photons is analyzed by inserting a rotating broadband polarizer (extinction ratio  $\sim 10^4:1$ ) in the collection path before the detectors.

## RESULTS AND DISCUSSION

Figure 2a reports the nonlinear emission spectrum of Antenna B, characterized by two narrow peaks around 518 nm and 777 nm that correspond to the THG (green) and the SHG (orange) emitted by the nanoantenna, respectively. To single out the individual SHG and THG contributions, although the incoherent luminescence emission from these nanostructures<sup>33</sup> is barely detectable, we select two narrow spectral regions (see arrows in Figure 2a) around the two emission peaks using band-pass filters. Figures 2b and 2c show the THG and SHG power curves acquired on both Antenna A and B. A comparison between the power curves indicates that the SHG has a quadratic dependence on the pump power, while the THG has an almost cubic power dependence. In addition, while THG in Antenna A is slightly higher than in the fully resonant Antenna B, for the SHG the behavior is the opposite. By considering the light collected and transmitted by the objective, the transmission of the optics and the quantum efficiency and the filling-factor of the SPAD unit, we estimate the effective THG (SHG) power emitted by Antenna B to be about 1.1 pW (3.9 pW) at  $\sim 0.2 \text{ GW/cm}^2$  pump fluency. This allows achieving maximum conversion efficiencies  $\eta_{\text{THG}} \approx 1.1 \times 10^{-8}$  and  $\eta_{\text{SHG}} \approx 3.9 \times 10^{-8}$  as well as nonlinear coefficients  $\gamma_{\text{THG}} = \frac{P_{\text{THG}}}{(P_{\text{FW}})^3} \approx 1.1 \text{ W}^{-2}$  and  $\gamma_{\text{SHG}} = \frac{P_{\text{SHG}}}{(P_{\text{FW}})^2} \approx 3.9 \times 10^{-4} \text{ W}^{-1}$ , where  $P_{\text{THG}}$ ,  $P_{\text{SHG}}$  and  $P_{\text{FW}}$  represent the THG, SHG and FW measured peak powers, respectively.

The polar plots representing the THG and SHG intensities for both antennas as a function of the rotation angle of the polarizer are shown in Figures 2d and 2e, respectively. While the main polarization axis of the SHG is orthogonal to the polarization axis of the FW light (i.e. parallel to the rod axis), as expected, the polarization state of the THG presents some unexpected features: (i) the maximum emission is obtained when the polarizer angle is set at about  $75^\circ$  and  $60^\circ$  for

antenna A and B, respectively, evidencing a significant tilt of the main polarization axis (15° and 30° for Antenna A and B, respectively) with respect to the linearly polarized pump electric field (see dark red double-headed arrow); (ii) the degree of linear polarization, which is related to the ratio between the maximum and the minimum of the intensity in the polar plot, is less pronounced than that of SHG in both antennas.

To investigate this peculiar behavior, we numerically evaluated the nonlinear polarized emission of the nanoantennas by means of full-wave finite-element simulations that consider the emission of the nanoantennas as the result of the three considered nonlinear phenomena. We first modeled the THG process (as sketched in Figure 3a) stemming from bulk  $\chi^{(3)}$  processes by considering gold as an isotropic material that induces a nonlinear polarization term at the third harmonic:  $\mathbf{P}_{3\omega} = \chi^{(3)}(\mathbf{E}_\omega \cdot \mathbf{E}_\omega)\mathbf{E}_\omega$  (in Gauss units)<sup>24-28</sup>. Concurrently, we described the emitted SHG (see Figure 3b) by considering the nonlinear surface currents at the second harmonic (SH),  $\mathbf{J}_{2\omega} = 2i\omega\mathbf{P}_{2\omega}$ , with  $\mathbf{P}_{2\omega} = \chi_{\perp\perp\perp}^{(2)}E_{\omega,\perp}^2\hat{\mathbf{n}}$  (where  $\hat{\mathbf{n}}$  is the normal to the metal surface).<sup>32,22,34-38</sup> To account for the experimental conditions, the electric far field generated by each phenomenon was projected over the polarizer axis and integrated over a collection angle corresponding to the numerical aperture of the objective. Figures 3d and 3e show the calculated polar plots for the bulk THG and surface SHG emission for both antennas (dark: Antenna A, bright: Antenna B). The intensities in each plot are normalized to that of Antenna B to highlight the relative changes in all the emission channels. These two plots represent a situation where the  $\chi^{(3)}$ -mediated THG stemming from the bulk and the  $\chi^{(2)}$ -mediated SHG originating from the surface of the nanostructures are completely uncoupled. A ready comparison with the experimental data highlights that, while the polarization behavior of the SHG (Figure 2e) is perfectly reproduced by a model based on a surface  $\chi_{\perp\perp\perp}^{(2)}$  process (Figure 3e), this is not the case for the THG originating

from a pure bulk  $\chi^{(3)}$  process. In fact, as already mentioned, the polarization behavior of the THG emitted by the investigated nanoantennas (Figure 2d) cannot be reconstructed with a pure bulk  $\chi^{(3)}$  model, which should display a polarized emission parallel to the FW polarization (Figure 3d) and with a degree of linear polarization higher than that of the SHG (Figure 3e).

To address this unexpected behavior and reproduce the experimentally-retrieved polarization state of the THG, we include in our model a cascaded second-order process, where a third-harmonic photon is generated by the coherent build-up of a FW photon and an SHG photon (see the scheme in Figure 3c), which eventually adds up to the THG related to pure bulk currents. Cascaded THG is commonly observed in non-centrosymmetric bulk crystals and, if properly optimized, allows boosting the THG efficiency in these media.<sup>39-42</sup> The presence of cascaded effects in THG seeded by SFG in plasmonic nanoantennas has been neglected in the literature thus far because of the large difference often reported between the SHG and THG emission yields. However, sizeable SFG has been recently reported for some specific plasmonic nanostructures<sup>13</sup> and the optimization of SFG through intrapulse phase engineering has been exploited to maximize SHG in plasmonic nanoantennas.<sup>43</sup> Here we consider a surface  $\chi_{\perp\perp\perp}^{(2)}$  term for SFG equivalent to that of SHG and, assuming both pump fields (FW and SH) are undepleted, we model the THG as the cascade of a SHG and a SFG process described by nonlinear surface currents,  $\mathbf{J}_{3\omega} = \chi_{\perp\perp\perp}^{(2)} E_{\omega,\perp} E_{2\omega,\perp} \hat{\mathbf{n}}$ .

Figure 3f displays the purely cascaded THG emission for both Antenna A (dark green) and B (light green) evaluated from numerical simulations. Even though the polarization state of SHG and  $\chi^{(3)}$ -mediated THG are very similar for both antenna geometries, cascaded THG features large variations, showing significant tilts of the main polarization axis with respect to the pump and a rather shallow degree of linear polarization. Moreover, the main polarization axis of the



cascaded THG emission is obtained in the far field appear to strongly differ for Antenna A and B (by about  $10^\circ$ ). Dissimilar (by about a factor 2) are also the maximum respective intensities. Thus, a significant contribution of this cascaded process would justify such a large tilt in the polarization axis of the total THG emission, including the different tilt angles for the two antennas as well as the depolarization with respect to the pump polarization state. For these reasons, we believe that the peculiar polarization state of the THG emission constitutes an undisputable evidence for the presence of the cascaded effect contributing to the THG from our nanostructures.

While recent theoretical models for  $\chi_{\perp\perp\perp}^{(2)}$ <sup>34,36</sup> were shown to be effective in reproducing several experimental findings<sup>36-38</sup>, the data reported in literature for the  $\chi^{(3)}$  value of gold are still subject to a large variability, due to the role played by the nonlinear incoherent effects and to the dependence of  $\chi^{(3)}$  on the resonant conditions as well as on the experimental configurations<sup>23-28</sup>. Moreover, the different origins of  $\chi^{(3)}$ -mediated and  $\chi^{(2)}$ -cascaded THG phenomena introduce further uncertainty in a quantitative comparison between the intensities of these two contributions. Therefore, to simulate the polar plots of the overall THG intensity that accounts for the contribution of both the volume third-order nonlinearity and the surface cascaded effect, we have first normalized the collected powers of the two contributions from both antennas to the power collected from Antenna B. Then we computed the total THG by integrating over the collection solid angle the intensity obtained by a linear combination of the far fields (in magnitude and phase) associated with the bulk- $\chi^{(3)}$ -mediated and the  $\chi^{(2)}$ -cascaded. Figures 4a and 4b show the comparison between the experimental THG polar plots (dots) for Antenna A and Antenna B (as in Figure 2d) and simulations, obtained using a linear combination of the relative numerical estimates (solid lines) as described above. The simulated polar plots for both

Antenna A and B well match the main polarization axis tilt for equal contributions ( $\sim 1:1$ ) of the fields stemming from the  $\chi^{(3)}$ -mediated and the  $\chi^{(2)}$ -cascaded THG. Conversely, the experimental SHG polar plots shown in Figs 4c and 4d (dots) are very well reproduced by simulating SHG as stemming solely from  $\chi_{\perp\perp\perp}^{(2)}$  surface contributions (solid lines), as expected in the case of undepleted pump.<sup>32</sup> The very good matching between experiments and simulations indicates that cascaded effects needs to be included to model the THG, in striking contrast with earlier findings reporting negligible interaction between SHG and THG in plasmonic nanoantennas. We also verified possible effects of the pump fluency on the cascaded THG by acquiring power-dependent emission polar plots (see Figure 5). As expected in an undepleted pump regime, the power-dependent polar plots for both THG (panel a) and SHG (panel b) do not display any significant modification in the polarized emission as a function of the pump fluency.

A quantitative numerical estimate of the overall THG yield, accounting for both the  $\chi^{(3)}$ -mediated and the  $\chi^{(2)}$ -cascaded processes, is hindered by the intrinsic uncertainty associated with the values of the second-order and especially third-order nonlinear coefficients of gold. Nevertheless, a scenario where  $\chi^{(3)}$ - and  $\chi^{(2)}$ -mediated processes at the nanoscale intervene on an equal footing in THG qualitatively requires comparable values of  $\chi^{(3)}$  and  $[\chi_{\perp\perp\perp}^{(2)}]^2$ . At a first glance, this might appear incompatible with the values determined for the nonlinear coefficients  $\gamma_{\text{THG}} \propto [\chi^{(3)}]^2$  – and  $\gamma_{\text{SHG}} \propto [\chi_{\perp\perp\perp}^{(2)}]^2$  – since  $\sqrt{\gamma_{\text{THG}}} \gg \gamma_{\text{SHG}}$ . However, one should bare in mind that in all plasmonic nanostructures the SH dipoles radiate in the far field with an efficiency that is much smaller than the one of the TH dipoles. Due to parity selection rules, in fact, low radiation efficiencies are often attained in the far field for SHG, because of the out-of-phase oscillation of the SH dipoles at the surface of the structure. This

leads to a complete suppression of the electric dipole emission mode of SH radiation in symmetric nanostructures, while this cancellation is only partially relieved in systems like our nanoantenna, where the symmetry is broken.<sup>45</sup> In both cases the SH radiation associated with the local oscillating dipoles in the nanostructure destructively interfere in the far field, resulting in small  $\gamma_{\text{SHG}}$  values even for a high  $\chi_{\perp\perp\perp}^{(2)}$ . Conversely, parity conservation in THG allows for the in-phase oscillation of dipoles either generated within the volume by third-order nonlinearities or at the surface by cascaded second-order nonlinear processes, resulting in a high radiation efficiency (and a high  $\gamma_{\text{THG}}$  value) for both phenomena. A remarkable consequence of this conclusion is that significant fingerprints associated with the  $\chi^{(2)}$ -cascaded THG process can be expected even in plasmonic nanostructures characterized by low SHG efficiencies, which further corroborates the importance of our findings.

## CONCLUSIONS

By studying the polarization state of the nonlinear emission in non-centrosymmetric gold antennas, we demonstrated that THG results from the combined action of a bulk  $\chi^{(3)}$ -mediated and a surface  $\chi^{(2)}$ -cascaded process. The latter is particularly sensitive to the antenna geometry, since it stems from a sizeable SFG process<sup>13</sup> between the intense SHG and the pump photons. This result sheds new light on the processes behind THG in plasmonic nanoantennas and allows envisaging the possibility of further enhancing this phenomenon in the near infrared, where the influence of interband transitions becomes negligible. The ability to tailor and optimize the SFG process in plasmonic nanoantennas also offers new degrees of freedom for the optimization and integration of multiple optical functionalities into complex photonic devices and metasurfaces.<sup>5</sup> This represents a key step towards the realization of nanoscale sensing devices and all-optical

devices for ultrafast switching and information processing in both classical and quantum optical systems at telecom wavelengths.

#### AUTHOR INFORMATION

##### **Corresponding Author**

\*michele.celebrano@polimi.it

##### **Author Contributions**

All authors contributed to writing the manuscript and they have all approved the final version.

‡These authors contributed equally. (match statement to author names with a symbol)

#### ACKNOWLEDGMENT

The authors would like to thank G. Cerullo for fruitful discussions. This work has been carried out in the framework of two COST Actions: COST MP1403 Nanoscale Quantum Optics and COST MP1302 Nanospectroscopy.

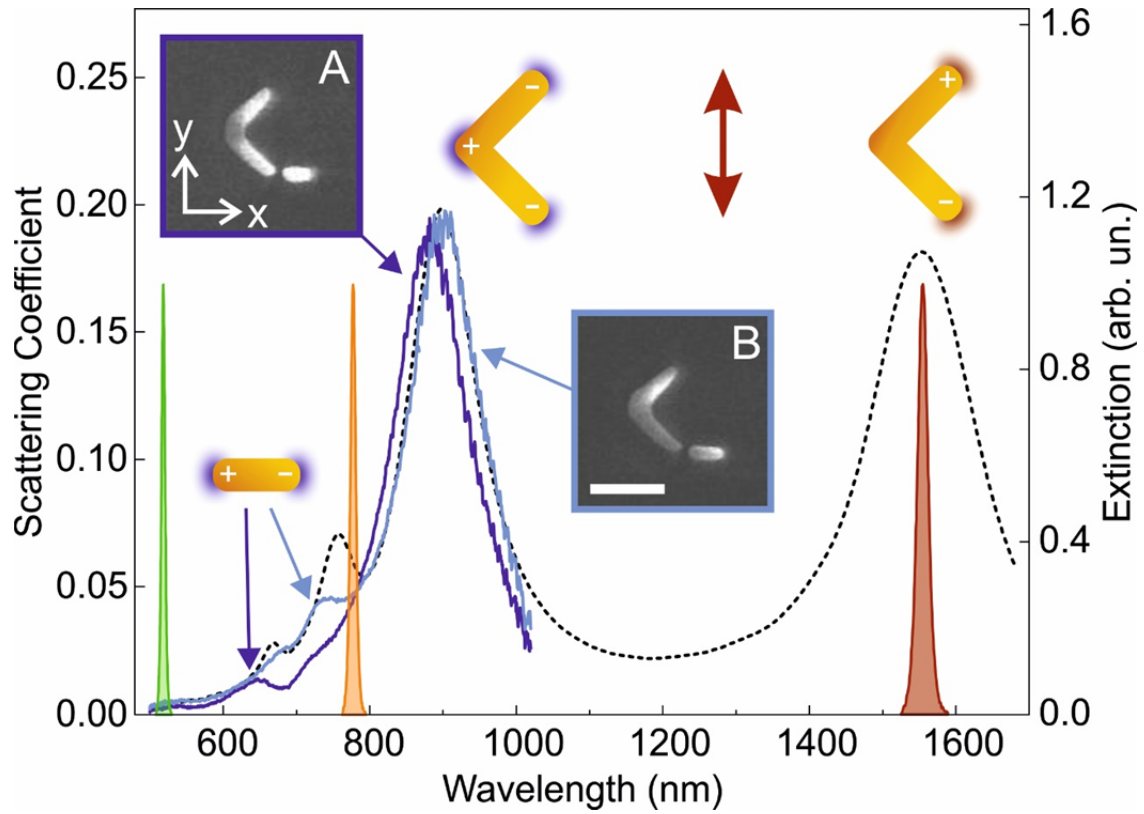


**Figure 1.** Whitelight spectra of the two investigated nanoantenna geometries: Antenna A (dark blue line) and Antenna B (light blue line). The dashed line is a finite-difference time-domain simulation of the scattering spectrum of Antenna B, highlighting the resonant behaviour at the FW around 1550 nm. The red filled curve represents the pump laser spectrum normalized to unity, while the orange and green filled curves indicate the respective hypotetic SHG and THG lines. The dark red double headed arrow represents the pump FW laser polarization. Insets: SEM images of Antenna A (dark blue) and Antenna B (light blue). The arm length of the V-shape of the nanostructure is about 160 nm, while the rod length is either 80 nm for Antenna A or 95 nm for Antenna B. The horizontal ruler corresponds to a length of 200 nm.

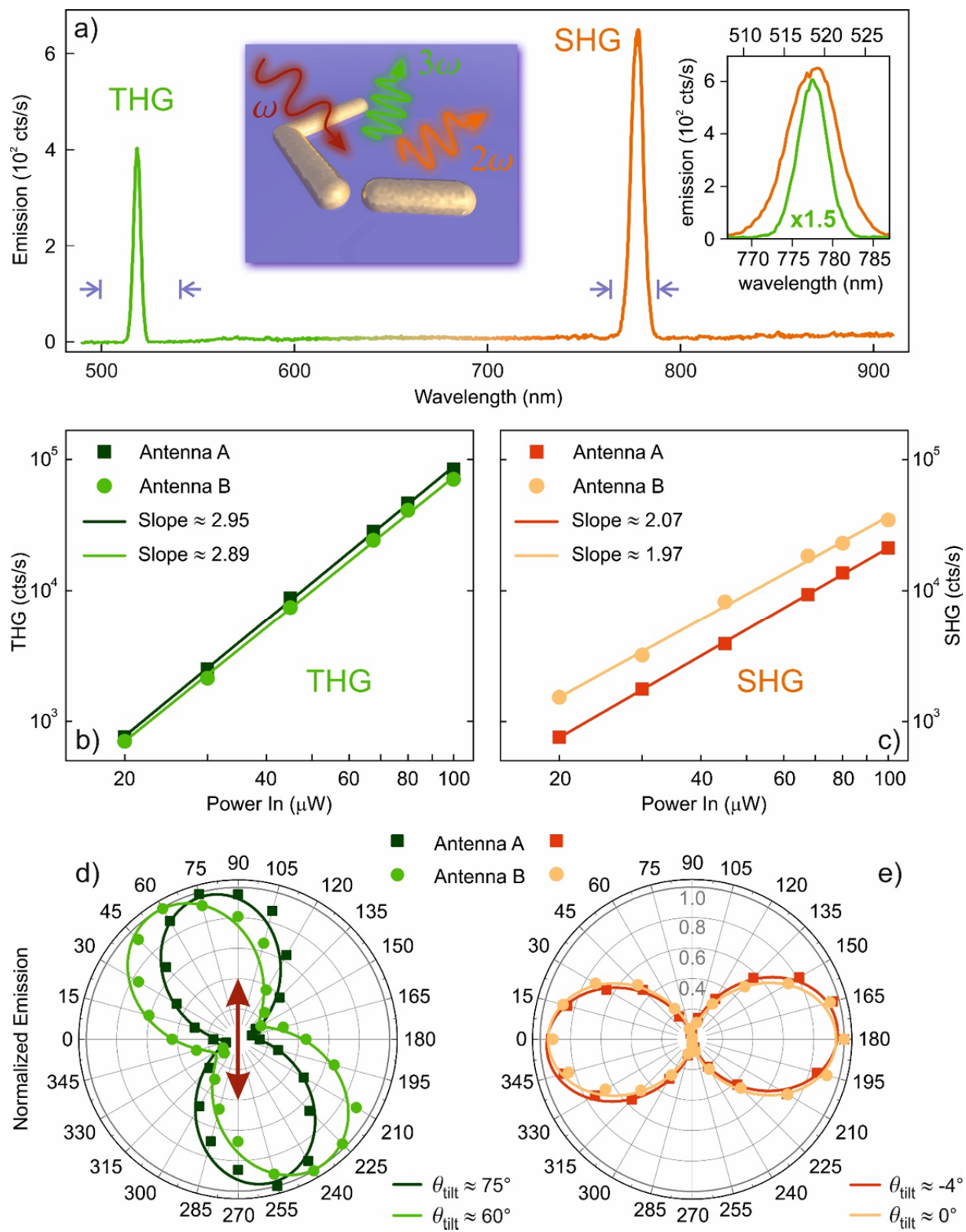


**Figure 2.** (a) Nonlinear emission spectrum of the double resonant Antenna B. The green side represents the visible part of the spectrum, while the orange side represents the NIR part. The light blue arrows indicate the rising and falling edges of the band-pass filters employed for the analysis of THG and SHG. The two filters are centered at 520 nm and 775 nm with bandwidths of 40 nm and 25 nm, respectively. Right inset: THG and SHG lines aligned and plotted on the same spectral width for comparison. The THG emission is peaked at 518 nm (linewidth  $\approx 4$  nm), while the SHG line is centered at 777 nm (linewidth  $\approx 7$  nm). Middle inset: picture of the nanoantenna with the color-coded harmonics involved in the processes. (b) THG (green) and (c) SHG (orange) intensities collected from Antenna A and Antenna B as a function of the input power. The solid lines represent linear fits to the experimental points. Darker lines correspond to the non-resonant Antenna A, while brighter lines to the doubly resonant Antenna B. (d, e) Polar plots of the normalized intensity emitted by THG (d) and SHG (e) for both antennas. The polar plot angle  $\theta$  is defined with respect to the horizontal  $x$  axis shown in Figure 1. Color codes are the same as for panels (b) and (c). Solid lines correspond to the best fit performed with the function  $A \cos^2(\theta - \theta_{\text{tilt}}) + B$ . The double-headed dark red arrow represents the direction of the pump linear polarization.

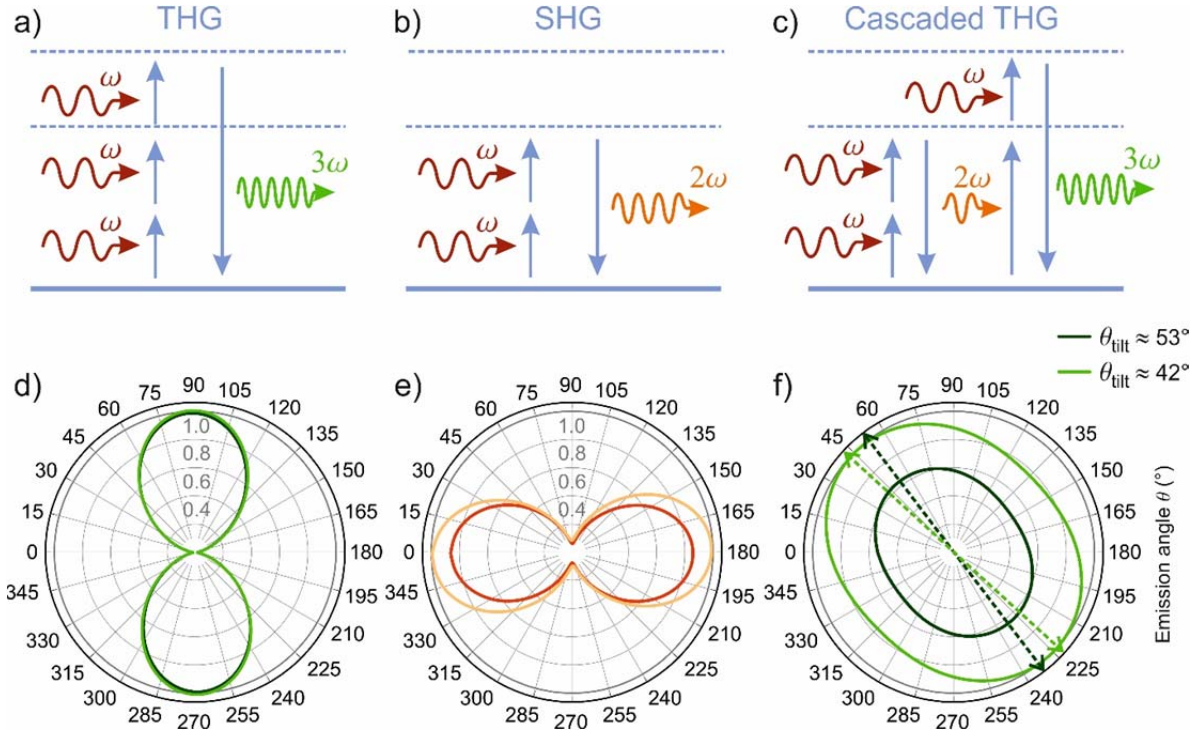


**Figure 3.** (a-c) Conversion schemes of the (a) THG, (b) SHG and (c) cascaded THG processes that are mediated by the nanoantenna. (d-f) Simulated emission polar plot for (d) purely bulk THG, (e) surface SHG, and (f) purely cascaded THG. The polar plot angle  $\theta$  is defined with respect to the horizontal  $x$  axis shown in Figure 1. The color code is the same as in Figure 2: dark lines refer to Antenna A, while bright lines refer to Antenna B. In each plot, the intensities are normalized to that of Antenna B. The dashed double-headed arrows in panel f indicate the linear polarization direction featuring the maximum emission for the cascaded THG process.



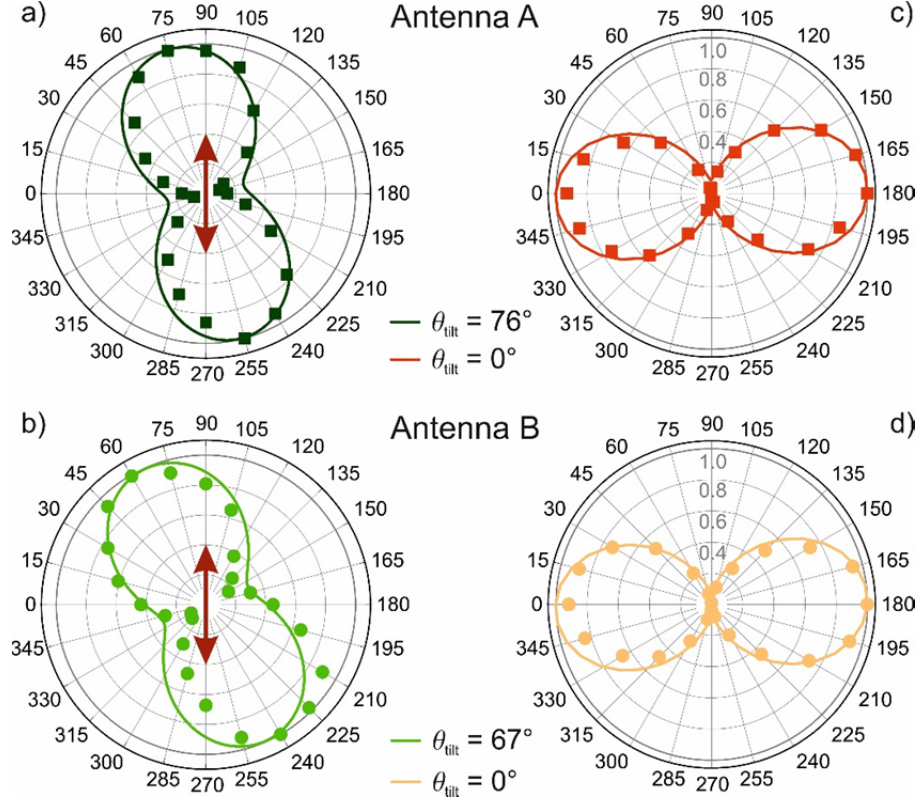


**Figure 4.** Normalized emission polar plots for the THG (a, b) and SHG (c, d) emitted by Antenna A and Antenna B, respectively. Solid lines in panel (a) and (b) represent the normalized emission polar plots simulated for the two geometries and obtained assuming a ratio between the bulk- $\chi^{(3)}$ -mediated and the cascaded THG equal to one for both geometries. The solid lines in panel (c) and (d) represent the normalized calculated SHG emission polar plots as obtained from a purely surface  $\chi^{(2)}$  contribution.  $\theta = 0^\circ$  corresponds to light polarization oriented parallel to the rod axis ( $x$  axis in Figure 1a).

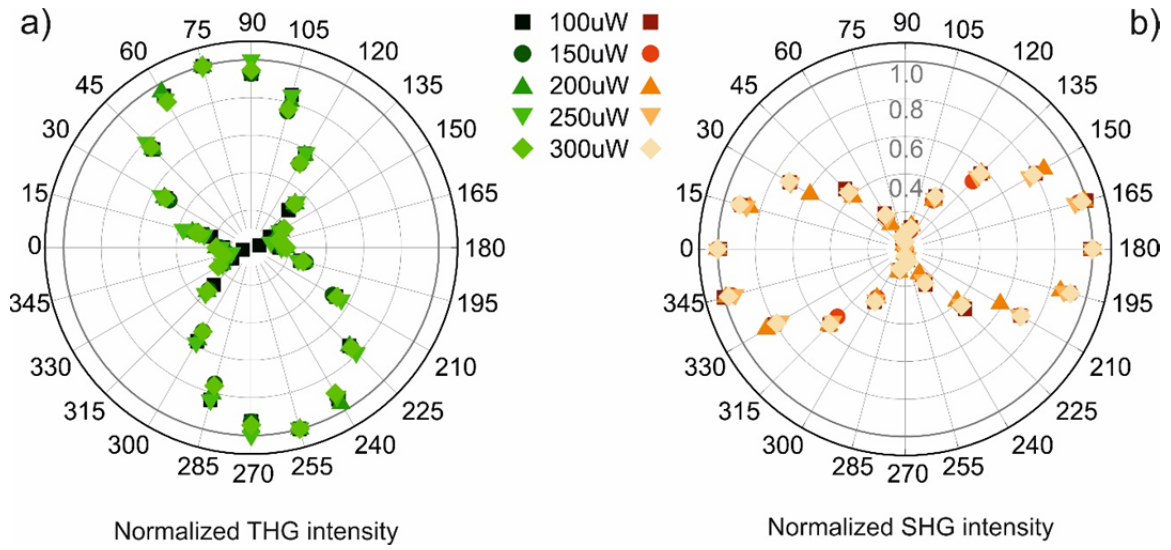


**Figure 5:** Power-dependent emission polar plots of (a) the THG and (b) the SHG for Antenna A. The peak emission intensities are normalized to 1 for all the incident powers for a ready comparison.

## REFERENCES

1. Smolyaninov II, Zayats AV, Davis CC. Near-field second harmonic generation from a rough metal surface. *Phys. Rev. B* 1997; **56**: 9290–9293.
2. Zayats AV, Kalkbrenner T, Sandoghdar V, Mlynek J. Second-harmonic generation from individual surface defects under local excitation. *Phys. Rev. B* 2000; **61**: 4545–4548.
3. Kauranen M, Zayats AV. Nonlinear Plasmonics. *Nature Photon.* 2012; **6**: 737–748.
4. Butet J, Brevet PF, Martin OJF. Optical Second Harmonic Generation in Plasmonic Nanostructures: From Fundamental Principles to Advanced Applications. *ACS Nano* 2015; **9**: 10545–10562.
5. Li G, Zhang S, Zentgraf T. Nonlinear photonic metasurfaces. *Nat. Rev. Mat.* 2017; **2**: 17010.
6. Maser A, Gmeiner B, Utikal T, Göttinger S, Sandoghdar V. Few-photon coherent nonlinear optics with a single molecule. *Nat. Photon.* 2016; **10**: 450–453.
7. Boyd RW. *Nonlinear Optics*, 3<sup>rd</sup> Ed. Cambridge: Academic Press, 2008; pp 79–84.
8. Novotny L, van Hulst NF. Antennas for light. *Nat. Photon.* 2011; **5**: 83–90.
9. Biagioni P, Huang J-S, Hecht B. Nanoantennas for visible and infrared radiation. *Rep. Prog. Phys.* 2012; **75**: 024402.
10. Hanke T, Cesar J, Knittel V, Trügler A, Hohenester U, Leitenstorfer A, Bratschitsch R. Efficient nonlinear light emission of single gold optical antennas driven by few-cycle near-infrared pulses. *Phys. Rev. Lett.* 2009; **103**: 257404.
11. Danckwerts M, Novotny L, Optical Frequency Mixing at Coupled Gold Nanoparticles. *Phys. Rev. Lett.* 2007; **98**: 026104.
12. Harutyunyan H, Volpe G, Quidant R, Novotny L. Enhancing the Nonlinear Optical Response Using Multifrequency Gold-Nanowire Antennas. *Phys. Rev. Lett.* 2012; **108**: 217403.
13. Sartorello G, Olivier N, Zhang J, Yue W, Gosztola DJ, Wiederrecht GP, Wurtz G, Zayats AV. Ultrafast Optical Modulation of Second- and Third-Harmonic Generation from Cut-Disk-Based Metasurfaces. *ACS Photon.* 2016; **3**: 1517–1522.
14. Hentschel M, Utikal T, Giessen H, Lippitz M. Quantitative Modeling of the Third Harmonic Emission Spectrum of Plasmonic Nanoantennas. *Nano Lett.* 2012; **12**: 3778–3782.
15. Dadap JJ, Shan J, Eienthal KB, Heinz TF. Second-Harmonic Rayleigh Scattering from a Sphere of Centrosymmetric Material. *Phys. Rev. Lett.* 1999; **83**: 4045.

16. Dadap JI, Shan J, Heinz TF. Theory of optical second-harmonic generation from a sphere of centrosymmetric material: small-particle limit. *J. Opt. Soc. Am. B* 2004; **21**: 1328.
17. Nappa J, Russier-Antoine I, Benichou E, Jonin Ch, Brevet PF. Second harmonic generation from small gold metallic particles: From the dipolar to the quadrupolar response *J. Chem. Phys.* 2006; **125**: 184712.
18. Ginzburg P, Krasavin A, Sonnefraud Y, Murphy A, Pollard RJ, Maier SA, Zayats AV. Nonlinearly coupled localized plasmon resonances: Resonant second-harmonic generation. *Phys. Rev. B* 2012; **86**: 085422.
19. Canfield BK, Husu H, Laukkanen J, Bai B, Kuittinen M, Turunen J, Kauranen M. Local Field Asymmetry Drives Second-Harmonic Generation in Noncentrosymmetric Nanodimers. *Nano Lett.* 2007; **7**: 1251–1255.
20. Gennaro SD, Rahmani M, Giannini V, Aouani H, Sidiropoulos TPH, Navarro-Cía M, Maier SA, Oulton RF. The Interplay of Symmetry and Scattering Phase in Second Harmonic Generation from Gold Nanoantennas *Nano Lett.* 2016; **16**: 5278–5285.
21. O’Brien K, Suchowski H, Rho J, Salandrino A, Kante B, Yin X, Zhang X. Predicting nonlinear properties of metamaterials from the linear response. *Nat. Mat.* 2015; **14**: 379–383.
22. Black LJ, Wiecha PR, Wang Y, De Groot CH, Paillard V, Girard C, Muskens OL, Arbouet A. Tailoring Second-Harmonic Generation in Single L-Shaped Plasmonic Nanoantennas from the Capacitive to Conductive Coupling Regime. *ACS Photon.* 2015; **2**: 1592–1601.
23. Hache F, Richard D, Flytzanis C, Krebig U. The Optical Kerr Effect in Small Metal Particles and Metal Colloids: The Case of Gold. *Appl. Phys. A* 1988; **47**: 347–357.
24. Conforti M, Della Valle G. Derivation of third-order nonlinear susceptibility of thin metal films as a delayed optical response. *Phys. Rev. B* 2012; **85**: 245423.
25. Lysenko O, Bache M, Lavrinenko A. Third-order susceptibility of gold for ultrathin layers. 2016; **41**: 317–320.
26. Boyd RW, Shi Z, De Leon I. The third-order nonlinear optical susceptibility of gold. *Opt. Comm.* 2014; **326**: 74–79.
27. Neira AD, Olivier N, Nasir ME, Dickson W, Wurtz GA, Zayats AV. Eliminating material constraints for nonlinearity with plasmonic metamaterials. *Nat. Comm.* 2015; **6**: 7757, DOI: 10.1038/ncomms8757.

28. Renger J, Quidant R, van Hulst N, Novotny L. Surface-Enhanced Nonlinear Four-Wave Mixing. *Phys. Rev. Lett.* 2010; **104**: 046803.
29. Knittel V, Fischer MP, Vennekel M, Rybka T, Leitenstorfer A, Brida D. *Phys. Rev. B* 2017; **96**: 125428.
30. Aouani H, Rahmani M, Navarro-Cía M, Maier SA. Third-harmonic upconversion enhancement from a single semiconductor nanoparticle coupled to a plasmonic antenna. *Nature Nanotech.* 2014; **9**: 290–294.
31. Metzger, B. et al. Doubling the efficiency of third harmonic generation by positioning ITO nanocrystals into the hot-spot of plasmonic gap-antennas. *Nano Lett.* 2014; **14**: 2867–2872.
32. Celebrano M, Wu X, Baselli M, Großmann S, Biagioni P, Locatelli A, De Angelis C, Cerullo G, Osellame R, Hecht B, Duò L, Ciccacci F, Finazzi M. Mode matching in multiresonant plasmonic nanoantennas for enhanced second harmonic generation. *Nat. Nanotechnol.* 2015; **10**: 412–417.
33. Biagioni P, Celebrano M, Savoini M, Grancini G, Brida D, Mátéfi-Tempfli S, Mátéfi-Tempfli M, Duò L, Hecht B, Cerullo G, Finazzi M. Dependence of the two-photon photoluminescence yield of gold nanostructures on the laser pulse duration. *Phys. Rev. B* 2009; **80**: 045411.
34. Sipe JE, So VCY, Fukui M, Stegeman GI. Analysis of 2nd-harmonic generation at metal-surfaces. *Phys. Rev. B* 1980; **21**: 4389-4402.
35. Zeng Y, Hoyer W, Liu J, Koch SW, Moloney JV. Classical theory for second-harmonic generation from metallic nanoparticles. *Phys. Rev. B* 2009; **79**: 235109.
36. Bachelier G, Butet J, Russier-Antoine I, Jonin C, Benichou E, Brevet P-F. Origin of the optical second-harmonic generation in spherical gold nanoparticles: local surface and non-local bulk contributions. *Phys. Rev. B* 2010; **82**: 235403.
37. De Corny ME, et al. Wave-mixing origin and optimization in single and compact aluminum nanoantennas. *ACS Photonics* 2016; **3**: 1840-1846.
38. Forestiere C, Capretti A, Miano G. Surface integral method for second harmonic generation in metal nanoparticles including both local-surface and nonlocal-bulk sources. *J. Opt. Soc. Am. B* 2013; **30**: 2355-2364.
39. Banks PS, Feit MD, Perry MD. High-intensity third-harmonic generation in beta barium borate through second-order and third-order susceptibilities. *Opt. Lett.* 1999; **24**: 4-6.

40. Mu X, Gu X, Makerov MV, Ding YJ, Wang J, Wei J, Liu Y. Third-harmonic generation by cascading second-order nonlinear processes in a cerium-doped KTiOPO<sub>4</sub> crystal. *Opt. Lett.* 2000; **25**: 117-119.
41. Sheng Y, Saltiel SM, Koynov K. Cascaded third-harmonic generation in a single short-range-ordered nonlinear photonic crystal. *Opt. Lett.* 2009; **34**: 656-658.
42. Solntsev AS, Sukhorukov AA, Neshev DN, Iliew R, Geiss R, Pertsch T, Kivshar YS. Cascaded Third Harmonic Generation in Lithium Niobate Nanowaveguides. *Appl. Phys. Lett.* 2011; **98**: 231110.
43. Accanto N, Nieder JB, Piatkowski L, Castro-Lopez M, Pastorelli F, Brinks D, van Hulst NF. Phase Control of Femtosecond Pulses on the Nanoscale using Second Harmonic Nanoparticles. *Light: Sci. Appl.* 2014; **3**: e143.
44. Zeng Y, Hoyer W, Liu J, Koch SW, Moloney JV. Classical theory for second-harmonic generation from metallic nanoparticles. *Phys. Rev. B* 2009; **79**: 235109.
45. Finazzi M, Biagioni P, Celebrano M, Duò L. Selection rules for second harmonic generation in nanoparticles. *Phys. Rev. B* 2007; **76**: 125414.